applied optics

Accurate testing of aspheric surfaces using the transport of intensity equation by properly selecting the defocusing distance

Peyman Soltani,[1] Ahmad Darudi,[1,*] George Nehmetallah,[2] Ali Reza Moradi,[3,4] and Javad Amiri[5]

[1]Physics Department, University of Zanjan, Zanjan 45195-313, Iran
[2]EECS Department, The Catholic University of America, 620 Michigan Ave., N.E., Washington, DC 20064, USA
[3]Department of Physics, Bilkent University, Cankaya, Ankara 06800, Turkey
[4]Optics Research Center, Institute for Advanced Studies in Basic Sciences, P.O. Box 45137-66731, Zanjan, Iran
[5]Department of Physics, Islamic Azad University Maragheh Branch, Maragheh, Iran
*Corresponding author: darudi@znu.ac.ir

Received 22 July 2016; revised 5 November 2016; accepted 8 November 2016; posted 8 November 2016 (Doc. ID 272215); published 9 December 2016

In the last decade, the transport of intensity has been increasingly used in microscopy, wavefront sensing, and metrology. In this study, we verify by simulation and experiment the use of the transport of intensity equation (TIE) in the accurate testing of optical aspheric surfaces. Guided by simulation results and assuming that the experimental setup parameters and the conic constants are known, one can estimate an appropriate defocusing distance Δz that leads to an accurate solution of the TIE. In this paper, this method is verified through the construction of a non-nulled experiment for testing the 2D profile of an aspheric surface. The theoretical method and experimental results are compared to validate the results. Finally, to validate the TIE methodology, the phase distribution obtained by TIE is compared with the phase distribution obtained by a Shack–Hartmann sensor.

OCIS codes: (120.0120) Instrumentation, measurement, and metrology; (150.6910) Three-dimensional sensing; (110.6880) Three-dimensional image acquisition.

https://doi.org/10.1364/AO.55.010067

1. INTRODUCTION

In the last two decades, compact and precise optical lens design systems became very important in the design of cameras, telescopes, microscopes, binoculars, laser printers, office copiers, endoscopes for minimally invasive surgery, laser-based optical readers for CD-ROM, product code laser scanners in supermarkets, ultra-precise projector lenses used in making integrated circuits, optical communication systems, and much more.

Aspheric surfaces are crucial components in the design of optical systems as they reduce the overall size and weight of optical components, resulting in a compact optical device. However, these advantages come with manufacturing and optical testing challenges which are still subject to ongoing research [1–6]. There are three main techniques for aspheric testing [1,7]: (a) profilometry techniques, which exhibit good range but lower sensitivity; (b) interferometry techniques, which have good sensitivity but less range (stitching and annual subaperture for large aspheres); and (c) geometric ray techniques, which are highly sensitive to zonal errors and figure asymmetries and can serve as a quick qualitative method to verify interferometric-based techniques. On the other hand, interferometry-based techniques are divided into two main categories: (a) null-testing (departure from an asphere) typically uses stigmatic imaging, aberration compensation, or aberration matching setups. Since the reflection beam from an aspheric surface exhibits large deviation in the optical path, null systems are usually employed [8]. (b) Non-null testing (mild departure from a sphere) typically uses slope measurement [7], non-null interferometry using an array of point sources [5], annual subaperture testing and stitching [9–14], and wavefront sensing using the Shack–Hartmann (SH) wavefront sensor which was used to measure rotationally symmetric aspheres [15].

In this paper, we adopt the non-null testing configuration for testing the wavefront of an aspheric surface through the use of the TIE method. The advantages of the TIE technique are accuracy, simplicity of optical setup, repeatability, high resolution, and speed, since there is no raster scanning involved as in profilometry techniques.

TIE was first suggested by Teague [16] and Sreibl [17]. The application of TIE in optical-quality testing of telescopes was suggested by Roddier *et al.* in 1993 [18,19]. During the last

three decades, several techniques were developed to solve the TIE. Some of the techniques were based on Green's functions [20], multigrid (MG) approach [21,22], and the Zernike polynomial expansion technique [23,24]. In the last decade, TIE has been used in several areas of optics, such as in adaptive optics and topography retrieval [24,25], quantitative phase-sensitive imaging for biological and bioengineering applications [26,27], optical measuring such as refractive index profile measurement and fringe analysis [28–30], and high speed optical tomography [31–33], just to name a few.

In a standard TIE optical setup, the phase of the optical beam can be recovered by measuring the intensity distributions at multiple defocused planes (minimum two) perpendicular to the propagation direction. The defocusing distance Δz separating these two planes is crucial to correctly estimate the derivative of the intensity along the propagation direction z.

In Section 2, we derive the relation between the phase and the derivative of the intensity. For a correct recovery of the phase, an accurate estimate of Δz is crucial. Note that there are two competing factors that should be considered. If the defocusing distance Δz is very small, the measurement noise might exceed the difference between the intensity distributions at the two defocused planes. If the defocusing distance is large, the signal will be less affected by measurement noise error. However, the estimate of the derivative becomes less accurate. Hence, the distance Δz has to be correctly estimated to obtain accurate results.

In the last decade, several techniques were proposed to find an optimized defocusing distance to improve the estimate of the axial intensity derivative from the intensity measurements in multiple planes. Some of these methods consider the effect of noise, higher-order derivatives, multiple intensities on equally or unequally spaced planes, or a combination of these factors [34–39].

In an earlier work, we assumed that the conic constant (CC) and radius of curvature (RC) of an aspheric surface are known, and a theoretical method was derived to accurately estimate the defocusing distance by investigating the error contribution due to Δz [40]. We concluded that an optimum value for Δz is related to the peak-to-valley (PV) of the phase distribution. The contribution of piston, tilt, and the quadric terms have been eliminated, for making accurate estimation of the PV [40].

In this paper, we demonstrate experimentally how to measure optical aspheric surfaces of known CC and RC. The accuracy of the measurement obtained using TIE is validated by using a Shack–Hartmann (SH) wavefront sensor.

2. TRANSPORT OF INTENSITY EQUATION

The TIE is derived starting from the Helmholtz equation: $(\nabla_\perp^2 + k^2)U(r) = 0$, that governs the propagation of the complex wave field $U(x, y, z) = E(x, y, z)\exp(jkz)$ in free space, where k is the wave number, and $\nabla_\perp^2 = (\frac{\partial^2}{\partial x^2} + \frac{\partial^2}{\partial y^2})$ is the transverse Laplacian operator. The TIE equation can be derived from the imaginary part of the Helmholtz equation under paraxial approximation and can be written as [22]

$$-k\frac{\partial I}{\partial z} = I\nabla^2\varphi(x, y, z) + \nabla I \nabla \varphi, \tag{1}$$

where φ is the unknown phase. The complex amplitude $E(x, y, z)$ is related to the intensity by

$$E(x, y, z) = \sqrt{I(x, y, z)}\,\exp(j\varphi(x, y, z)). \tag{2}$$

Based on Eq. (1), the TIE equation relates the axial change (derivative) $\partial I/\partial z$ of the transverse spatial intensity distribution to the spatial intensity $I(x, y, z)$ and phase $\phi(x, y, z)$. In a first-order approximation, the derivative is approximated as the difference between two measured intensities divided by Δz, and can be written as

$$\frac{\partial I(x, y)}{\partial z} \approx \frac{I(x, y, \Delta z/2) - I(x, y, -\Delta z/2)}{\Delta z}. \tag{3}$$

One of the simplest and widely used techniques to solve the TIE is based on the Fourier transform iterative technique [18]. In this technique, it is assumed that the intensity distribution at the pupil plane ($z_0 = 0$) is approximately constant ($\nabla I = 0$). Figure 1(a) below shows the location of the pupil plane. Hence, Eq. (1) can be converted into a Poisson equation [27]:

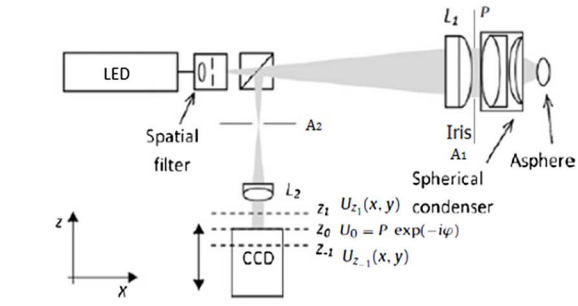

(a)

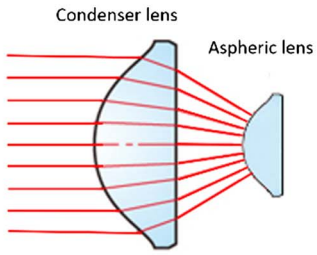

(b)

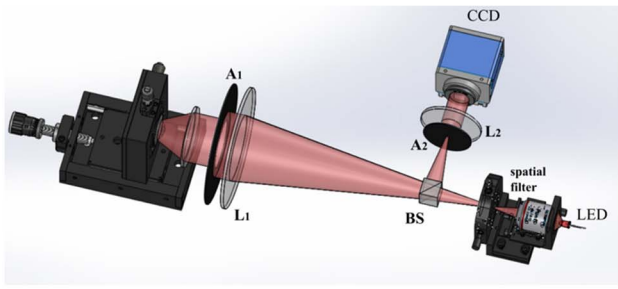

(c)

Fig. 1. (a) Schematic of the simulated non-null setup for aspheric surface testing. The peak-to-valley (PV) of the phase distribution is controlled by the size of the pupil P of the system; (b) cartoon showing the center of curvature of the asphere coinciding with the focal plane of the condenser; and (c) the 3D view of the non-null test configuration.

$$\nabla_{\perp}^{2}\varphi(x,y,z) = -\left(\frac{2k}{\Delta z}\right)S, \tag{4}$$

where S denotes the signal function and is given by

$$S = \frac{I(x,y,z_0+\Delta z/2) - I(x,y,z_0-\Delta z/2)}{I(x,y,z_0+\Delta z/2) + I(x,y,z_0-\Delta z/2)}, \tag{5}$$

where $I(x,y,z_0-\Delta z/2)$ and $I(x,y,z_0+\Delta z/2)$ represent the intensity distributions along the z axis at the overfocused and underfocused planes of the system, respectively. These two planes are separated by the defocusing distance Δz. Note that Eq. (4) can be solved using the Fourier transform technique:

$$\varphi(x,y,z) = -\left(\frac{2k}{\Delta z}\right)\mathcal{F}^{-1}\left\{\frac{\mathcal{F}\{S\}}{k_x^2+k_y^2}\right\}, \tag{6}$$

where $\mathcal{F}$ and $\mathcal{F}^{-1}$ are the forward and inverse 2D Fourier transform; k_x and k_y are the spatial frequencies in the Fourier domain. The $(k_x^2+k_y^2)$ term is due to the Laplacian operator in the frequency domain.

3. EXPERIMENTAL SETUP, RESULTS, AND SIMULATION

The methodology for testing the aspheric surface using TIE is discussed in this section. This section is divided into four parts. The experimental setup of the non-null test configuration is discussed in detail in the first part. In the second part, and in order to obtain a good estimate of the defocusing distance, we simulate the propagation of the complex fields for different PVs. As a result, the intensities before and after the image plane are computed using Fresnel propagation. The phase aberration due to the simulated aspheric surface is then computed using TIE.

In the third part, and guided by simulation results, experimental results are shown. In the fourth part, the experimental results obtained using TIE are compared with the results obtained by a Hartmann wavefront sensor for validation purposes.

A. Experimental Setup

In this section, the experimental setup of the non-null test configuration is discussed and the TIE methodology outlined in Section 2 is used for testing the 2D topography of an asphere. In the non-null configuration, the phase aberration of the reflected wave due to the aspherical surface is the departure from the phase of a known spherical surface, and hence is given by

$$\varphi(r) = \varphi_{\text{asph}}(r) - \varphi_{\text{sph}}(r), \tag{7}$$

where $\varphi_{\text{sph}}(r)$ and $\varphi_{\text{asph}}(r)$ are the phases of the spherical and aspheric surfaces, respectively. Note that φ_{sph} is the compensated part of the phase due to the condenser lens. This means that in the experimental setup, the center of curvature of the asphere should coincide with the focal plane of the condenser lens, as shown in Fig. 1(b). If the aspheric surface parameters are known, the analytic formula of the phase can be written as

$$\varphi_{\text{asph}}(r) = 2\left[k\frac{r^2}{R+\sqrt{R^2-(K+1)r^2}} + \sum_{i=1}^{n} A_i\varphi(r^{2i})\right], \tag{8}$$

where R is the radius of curvature at the vertex of the aspheric surface, K is the conic constant, k is the wave number, $r = \sqrt{x^2+y^2}$ is the radial distance from the optical axis, and $A_i\varphi(r^{2i})$ are the higher-order aspheric terms. In this study, and for the sake of simplicity, we neglect the higher-order aspheric terms.

Figure 1(a) shows a schematic of the simulated non-null setup for aspheric surface testing. A partially coherent 470 nm LED source is used for illumination. The light passes through a spatial filter with a pinhole of 100 μm diameter. The beam is collimated by a high-quality double lens $L_1(f = 500\text{ mm})$. Then, the collimated beam illuminates the aspheric surface target assembly through a spherical condenser. The magnification of 1:7.2 is introduced by a collimating lens L_2 in front of the CCD camera, which captures the overfocused (z_{-1} plane) and underfocused (z_1 plane) intensities. The CCD camera used is 640 × 480 pixel array size (DMK 21AF04 camera by Imaging Source), where each pixel size is $\Delta x = 5.6$ μm. The CCD is mounted on a translation stage controlled by a stepper motor of precision accuracy of 0.048 mm. Another x-y manual translation stage and a tip/tilt mount are also used for adjusting the position of the aspheric surface. Note that the peak-to-valley (PV) of the phase distribution is controlled by the size of the pupil P of the system (A_1). Figure 1(c) shows a 3D view of the same non-null test setup [41].

In the experimental setup, an aspheric surface of known conic constant $K = -0.012$ and radius of curvature $R = 15$ mm is used. The diameter of the tested surface is 16.8 mm. The pupil size can be reduced by using an iris (A_1) placed before the condenser lens, as shown in Fig. 1(a). To obtain a precise estimate of the axial derivative of the intensity, several experiments are carried out. Guided by simulation results, a series of experiments show that the optimal value of the defocusing distance is related to the PV of the aspheric phase distribution.

B. Simulation

The simulation is conducted as follows: for each of the five pupil diameters [24, 21, 19, 16.8, and 15] mms corresponding to PVs [255.9, 112.6, 68, 35, and 20.6] rad, the defocusing distance Δz is varied from 1.0 to 400 mm. In order to be able to quantify the percentage of the error between the predefined wavefront [computed from Eqs. (7) and (8)] and reconstructed one using TIE [Eq. (6)] in each of the cases above, the root mean square (RMS) error was chosen as a figure of merit, and can be written as [40]

$$\text{ER} = \frac{\sqrt{\iint(\varphi_{\text{TIE}}-\varphi_i)^2 dA}}{\sqrt{\iint\varphi_{\text{TIE}}^2 dA}}, \tag{9}$$

where φ_{TIE} is calculated from TIE, φ_i is the predefined phase distribution from Eq. (8), and dA is the elemental area. The results are shown in Fig. 2. The cross, dashed-dotted, dashed, solid, and dotted curves are the values of ER versus Δz for different values of PV. From Fig. 2, one can easily deduce that the RMS error between the solution from TIE and the real value strongly depends on Δz. Also, one can deduce that for each of the PV values, the TIE solution is not monotonic, but attains a minimum value in a narrow band of Δz. This narrow band is different for different values of PV. One can also deduce that the defocusing distance value in which the narrow band exists, and its width are inversely proportional to the value of PV. Hence, larger PVs needs smaller defocusing distances.

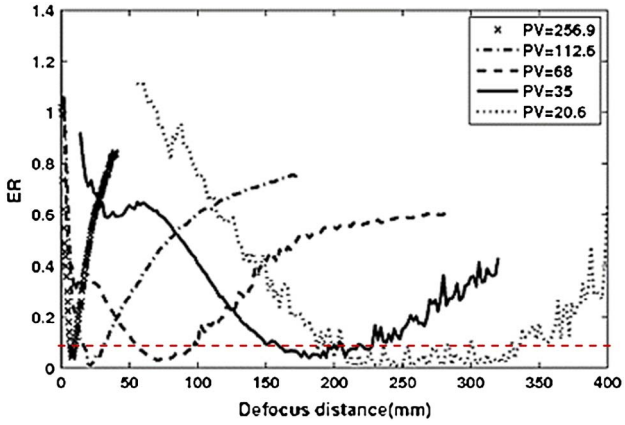

Fig. 2. Simulation results showing the root mean square error ER versus defocusing distances Δz for several values of PV.

In Fig. 3, the solid blue line shows the simulated optimum data of Δz (which correspond to the narrow band region around the minimum of ER) versus PV deduced from the data shown in Fig. 2. The error bars illustrate the width of the narrow band regions from Fig. 2. As an example, in Fig. 3 the narrow band region cut-off is chosen to be at ER = 0.1 (see dashed red line in Fig. 2).

C. Experimental Results

The simulation results shown in Fig. 3 serve as a guiding basis for estimating the correct range of the defocusing distance for a certain PV value. This estimate should be used while conducting the experiment in order to achieve low ER. The experimental setup shown in Fig. 1(c) is used to test an aspheric surface having the same parameters as those used in the simulation. The illumination light from an LED passes through a spatial filter which is collimated by lens L_1 before converging on the aspheric surface by a condenser lens (see Fig. 1). The reflected light from the aspheric surface is reflected from a beam splitter (BS) and then collimated by lens L_2. An aperture stop (A_2) situated at the focal point before lens L_2 is used to only pass the reflection from the aspheric surface to be tested.

The first step is to record the overfocused and underfocused intensity distributions on both sides of the virtual image plane

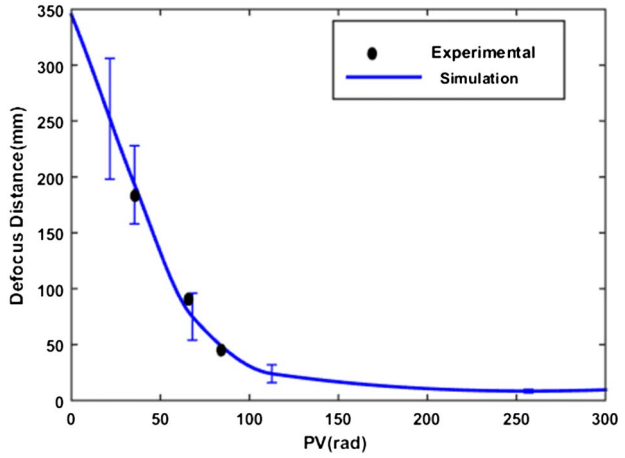

Fig. 3. Optimum value (min ER) of the defocusing distance Δz versus PV. Solid curve is the simulation and the black (o) marker is the experimental data. The vertical bars show the range of the narrow band when the minimum ER < 0.1.

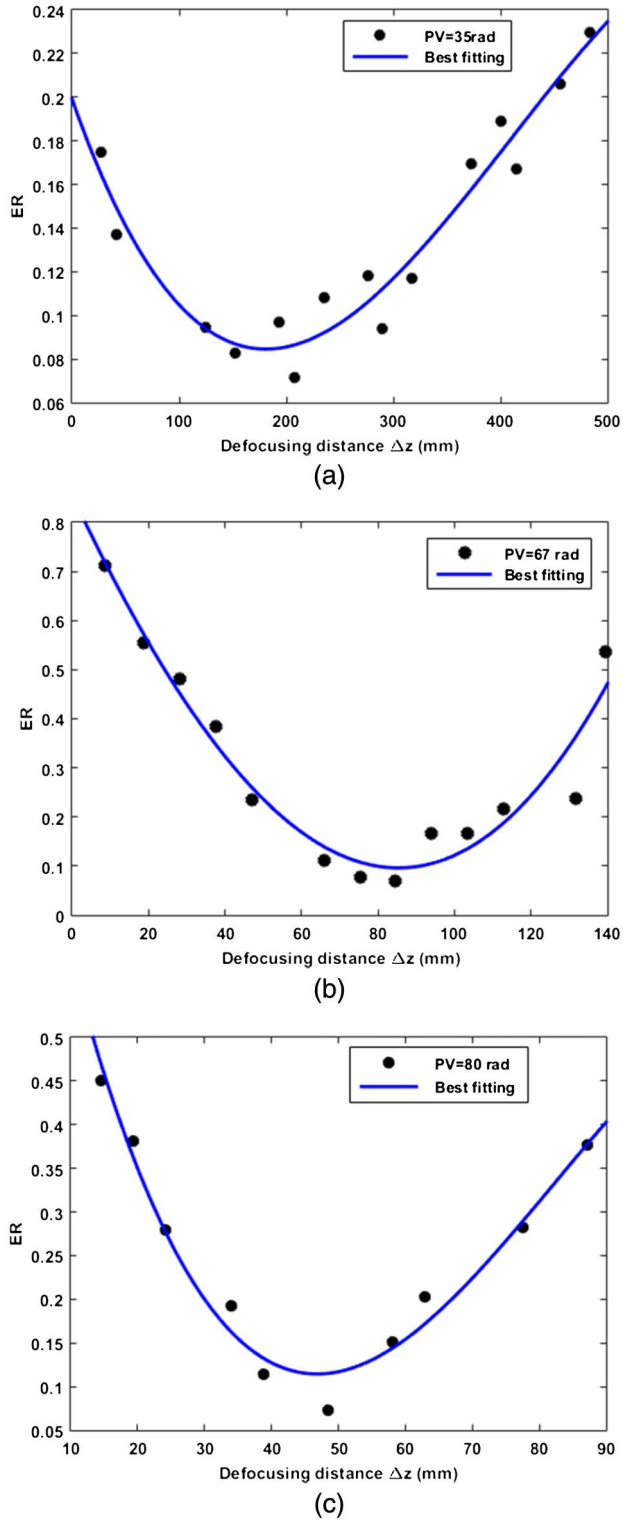

Fig. 4. Root mean square error ER of the experimental measurements at different defocusing distances Δz for (a) PV = 35 rad, (b) 67 rad, and (c) 80 rad, respectively.

with separation $\Delta z' = (3.5 + 2.5 \times \mathrm{m})$ mm, where m = 1, 2, 3, etc. The equivalent separation distances in object space are given by $\Delta z = \Delta z' \times M$, where $M = 7.2$ is the magnification of the system. The second step is to compute the signal function S using Eq. (5). In step 3, the Fourier method is implemented to solve the TIE to obtain the experimental phase value due to the aspheric surface. The experimentally calculated and simulated phase distributions are substituted in Eq. (9) to find the error, ER.

Figures 4(a), 4(b), and 4(c) illustrate the RMS error ER versus the defocusing distances Δz, for PV = 35 rad, 67 rad, and 80 rad, respectively. Three third-order polynomials are fitted to the data points to find the minimums of the curves which give the optimal separation distances of $\Delta z = 190$ mm, 85 mm, and 50 mm, respectively. These defocusing values are marked by black circular markers in Fig. 3 above, which is clearly within the prediction of the simulation results. It is worth noting that aspherical wavefront slopes with high PV are out of Shack–Hartman dynamic range.

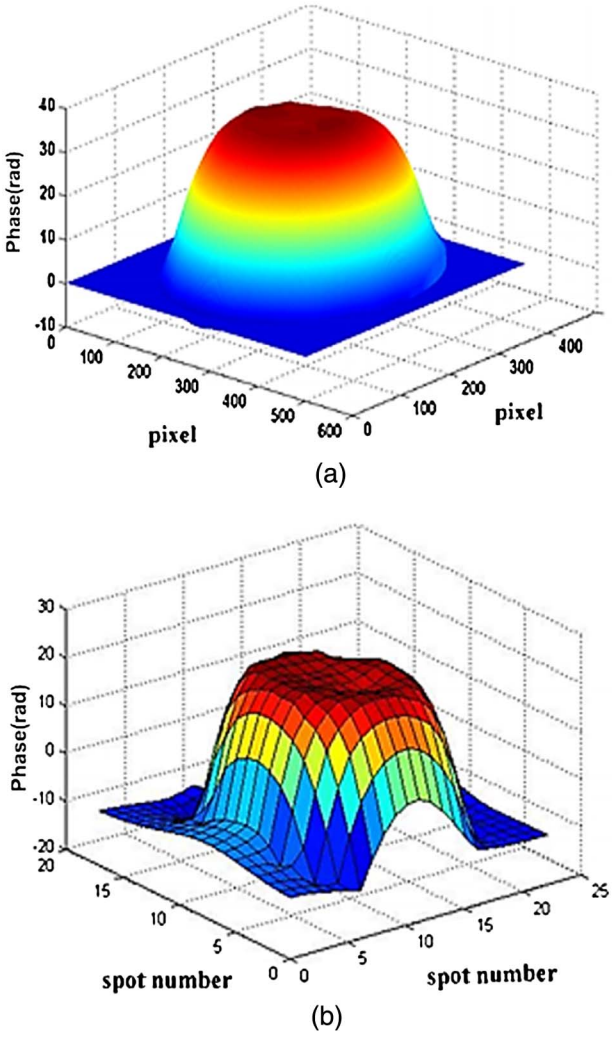

Fig. 5. Phase distribution calculated using (a) TIE and (b) the SHWS for the case when PV = 35 rad.

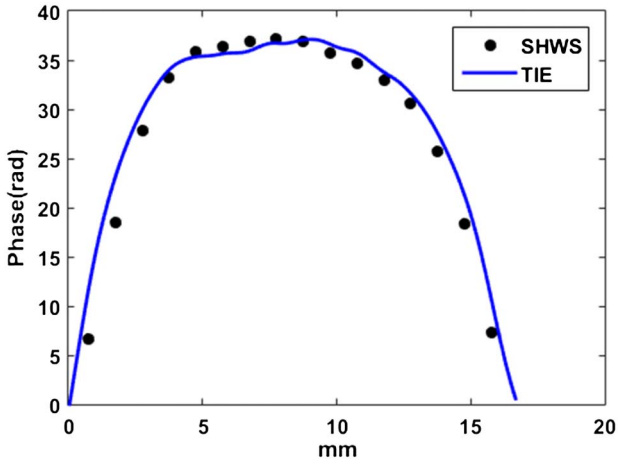

Fig. 6. Phase distribution profile passing through the center of the 3D phase distributions of Fig. 5. Solid line profile is obtained by TIE and the star marker profile is obtained from SHWS for the case where PV = 35 rad.

D. Result Validation Using the Shack–Hartmann Wavefront Sensor

For validation purposes, and in order to evaluate the accuracy of the TIE solution at a given defocusing distance Δz, a Shack–Hartmann wavefront sensor (SHWS) is used. The SHWS is mounted instead of the CCD camera in the experimental setup in Fig. 1. The SHWS sensor consists of a camera model MLA150-7AR and a 50×50 microlens array of overall size 10×10 mm from Thorlabs. Each lenslet has a focal length of $f = 6.7$ mm and a diameter of 150 μm. To calculate the Hartmann vectors, the centroids of the recorded spots on the SHWS camera are analyzed by subtracting the SH grid coordinates of the object beam from that of the reference beam. The wavefront phase distribution is then reconstructed by integration using Hudgins methods.

For the case of PV = 35 rad, Figs. 5(a) and 5(b) show the reconstructed phase distributions using TIE and the SHWS, respectively. As shown in Fig. 5, the results obtained from the SHWS are in excellent agreement with those measured by the TIE technique. The solid blue line and the SHWS data points (black circles) for the case of PV = 35 rad in Fig. 6 shows two profiles of phase distributions that pass through the center of the 3D phase distributions of Figs. 5(a) and 5(b), respectively. It is obvious that the TIE has a higher resolution than SHWS, which is a major advantage of the TIE technique.

We should note that the wavefront RMS error measured by the SHWS is about 10 nm. The definition of error given in Eq. (9) is equivalent to the ratio between the RMS of the noise to the average of the signal. Therefore, for a wavefront of nominal value of PV of 40 rad, (roughly 20 rad mean signal value) the ER is 0.006, which is far smaller than TIE errors.

4. CONCLUSION

In this paper, a non-nulled experiment was constructed for testing an aspheric surface with known conic constant (CC) and radius of curvature (RC) parameters. We have shown experimentally that the solution using the TIE method depends

on the defocusing distance Δz. We verified that the TIE simulation results serve as a guide to predict the best defocusing distance to measure the topography of an aspheric surface with known parameters. Using simulation, a proper defocusing distance Δz is estimated to be about 190 mm for PV = 35 rad, leading to an accurate solution of the TIE. Two more experiments were also conducted for two other values of PV = 67 rad and 80 rad, leading roughly to the defocusing distances of $\Delta z = 85$ mm and 50 mm, respectively, which are in agreement with predictions of simulation results shown in Fig. 3. For verification of the solution, a Shack–Hartmann wavefront sensor was also employed. The phase distribution of the SHWS is in agreement with the results obtained by TIE.

Due to the different sources of error in SHWS and TIE techniques, some deviation of both plots in Fig. 6 is expected. The SHWS cannot recover the high spatial frequency components of the wavefront, and the recovered slopes of the wavefront are an average over the micro-lens diameter. However, the accuracy of SHWS is higher than that of TIE by an order of magnitude. Generally, the solution using TIE for a wavefront with a wide range of spatial frequencies is also not very accurate. The small defocusing distance is suitable for recovering the high frequency wavefront components and vice versa for low frequencies [42].

REFERENCES

1. J. C. Wyant and V. P. Bennett, "Using computer generated holograms to test aspheric wavefronts," Appl. Opt. **11**, 2833–2839 (1972).
2. A. Ono and J. C. Wyant, "Aspherical mirror testing using a CGH with small errors," Appl. Opt. **24**, 560–563 (1985).
3. J. H. Burge, "Fizeau interferometry for large convex surfaces," Proc. SPIE **2536**, 127–138 (1995).
4. T. Kim, J. H. Burge, Y. Lee, and S. Kim, "Null test for a highly paraboloidal mirror," Appl. Opt. **43**, 3614–3618 (2004).
5. E. Garbusi, C. Pruss, and W. Osten, "Interferometer for precise and flexible asphere testing," Opt. Lett. **33**, 2973–2975 (2008).
6. M. Kino and M. Kurita, "Interferometric testing for off-axis aspherical mirrors with computer generated holograms," Appl. Opt. **51**, 4291–4297 (2012).
7. P. Stahl, "Aspheric surface testing techniques," in *Fabrication and Testing of Aspheres*, OSA Trends in Optics and Photonics (Optical Society of America, 1999), Vol. **24**.
8. D. Malacara, *Optical Shop Testing*, 3rd ed. (Wiley, 2007).
9. P. Murphy, J. Fleig, G. Forbes, D. Miladinovic, G. DeVries, and S. O'Donohue, "Subaperture stitching interferometry for testing mild aspheres," Proc. SPIE **6293**, 62930J (2006).
10. M. F. Kuchel, "Absolute measurement of rotationally symmetrical aspheric surfaces," in *OSA Topical Meeting on Optical Fabrication and Testing*, Rochester, USA, 2006, paper OFTuB5.
11. Y. Wen, H. Cheng, H. Y. Tam, and D. Zhou, "Modified stitching algorithm for annular subaperture stitching interferometry for aspheric surfaces," Appl. Opt. **52**, 5686–5694 (2013).
12. J. E. Greivenkamp and R. O. Gappinger, "Design of a non-null interferometer for aspheric wave fronts," Appl. Opt. **43**, 5143–5151 (2004).
13. Y.-M. Liu, G. N. Lawrence, and C. L. Koliopoulos, "Subaperture testing of aspheres with annular zones," Appl. Opt. **27**, 4504–4513 (1988).
14. M. Melozzi, L. Pezzati, and A. Mazzoni, "Testing aspheric surfaces using multiple annular interferograms," Opt. Eng. **32**, 1073–1079 (1993).
15. J. Pfund, N. Lindlein, and J. Schwider, "Non-null testing of rotationally symmetric aspheres: a systematic error assessment," Appl. Opt. **40**, 439–446 (2001).
16. M. R. Teague, "Irradiance moments: their propagation and use for unique retrieval of phase," J. Opt. Soc. Am. **72**, 1199–1209 (1982).
17. N. Streibl, "Phase imaging by the transport equation of intensity," Opt. Commun. **49**, 6–10 (1984).
18. F. Roddier and C. Roddier, "Wavefront reconstruction using iterative Fourier transforms," Appl. Opt. **30**, 1325–1327 (1991).
19. C. Roddier and F. Roddier, "Wave-front reconstruction from defocused images and the testing of ground-based optical telescopes," J. Opt. Soc. Am. A **10**, 2277–2287 (1993).
20. M. R. Teague, "Deterministic phase retrieval: a Green's function solution," J. Opt. Soc. Am. **73**, 1434–1441 (1983).
21. L. J. Allen and M. P. Oxley, "Phase retrieval from series of images obtained by defocus variation," Opt. Commun. **199**, 65–75 (2001).
22. W. Xiao, M. Heng, and Z. Dazun, "Phase retrieval based on intensity transport equation," Acta Opt. Sin. **27**, 2117–2122 (2007).
23. T. E. Gureyev, A. Roberts, and K. A. Nugent, "Phase retrieval with the transport-of-intensity equation: matrix solution with use of Zernike polynomials," J. Opt. Soc. Am. **12**, 1932–1941 (1995).
24. S. V. Pinhasi, R. Alimi, L. Perelmutter, and S. Eliezer, "Topography retrieval using different solutions of the transport intensity equation," J. Opt. Soc. Am. A **27**, 2285–2292 (2010).
25. V. Orlav, E. Luna, and E. Orlova, "Optimal defocus distance for testing the 2.1 m telescope at San Pedro Martir," Appl. Opt. **44**, 5169–5172 (2005).
26. S. Bajt, A. Barty, K. A. Nugent, M. McCartney, M. Wall, and D. Paganin, "Quantitative phase-sensitive imaging in a transmission electron microscope," Ultramicroscopy **83**, 67–73 (2000).
27. J. Frank, J. Matrisch, J. Horstmann, S. Altmeyer, and G. Wernicke, "Refractive index determination of transparent samples by noniterative phase retrieval," Appl. Opt. **50**, 427–433 (2011).
28. A. Darudi, R. Shomali, and M. T. Tavassoly, "Determination of the refractive index profile of a symmetric fiber preform by the transport of intensity equation," Opt. Laser Technol. **40**, 850–853 (2008).
29. J. Amiri, A. Darudi, S. Khademi, and P. Soltani, "Application of transport of intensity equation in fringe analysis," Opt. Lett. **39**, 2864–2867 (2014).
30. P. Soltani, A.-R. Moradi, A. Darudi, and R. Shomali, "High resolution optical surface testing using transport of intensity equation," Proc. SPIE **8785**, 87851K (2013).
31. S. Memarzadeh, P. P. Banerjee, and G. Nehmetallah, "Noninterferometric tomographic reconstruction of 3D static and dynamic phase and amplitude objects," Proc. SPIE **9117**, 91170M (2014).
32. T. C. Nguyen, G. Nehmetallah, A. Darudi, and P. Soltani, "3D high speed characterization of phase and amplitude objects using the transport of intensity equation," Proc. SPIE **9495**, 949512 (2015).
33. T. Nguyen, G. Nehmetallah, D. Tran, A. Darudi, and P. Soltani, "Fully automated, high speed, tomographic phase object reconstruction using the transport of intensity equation in transmission and reflection configurations," Appl. Opt. **54**, 10443–10453 (2015).
34. L. Waller, L. Tian, and G. Barbastathis, "Transport of Intensity phase-amplitude imaging with higher order intensity derivatives," Opt. Express **18**, 12552–12561 (2010).
35. D. Paganin, A. Barty, P. J. McMahon, and K. A. Nugent, "Quantitative phase-amplitude microscopy, III: the effect of noise," J. Microsc. **214**, 51–61 (2004).
36. M. Soto, E. Acosta, and S. Ríos, "Performance analysis of curvature sensors: optimum positioning of the measurement planes," Opt. Express **11**, 2577–2588 (2003).
37. M. Soto and E. Acosta, "Improved phase imaging from intensity measurements in multiple planes," Appl. Opt. **46**, 7978–7981 (2007).
38. B. Xue, S. Zheng, L. Cui, X. Bai, and F. Zhou, "Transport of intensity phase imaging from multiple intensities measured in unequally-spaced planes," Opt. Express **19**, 20244–20250 (2011).
39. S. Zheng, B. Xue, W. Xue, L. Cui, X. Bai, and F. Zhou, "Transport of intensity phase imaging from multiple noisy intensities measured in unequally-spaced planes," Opt. Express **20**, 972–986 (2012).
40. R. Shomali, A. Darudi, and S. Nasiria, "Application of irradiance transport equation in aspheric surface testing," Optik **123**, 1282–1286 (2012).
41. P. Soltani, A. Darudi, A. Reza Moradi, J. Amiri, and G. Nehmetallah, "A guide to properly select the defocusing distance for accurate solution of transport of intensity equation while testing aspheric surfaces," Proc. SPIE **9868**, 986804 (2016).
42. K. Ishizuka and B. Allman, "Phase measurement of atomic resolution image using transport of intensity equation," J. Electron. Microsc. **54**, 191–197 (2005).